J. Fluid Mech. (2025), *vol.* 1022, A30, doi:10.1017/jfm.2025.10654

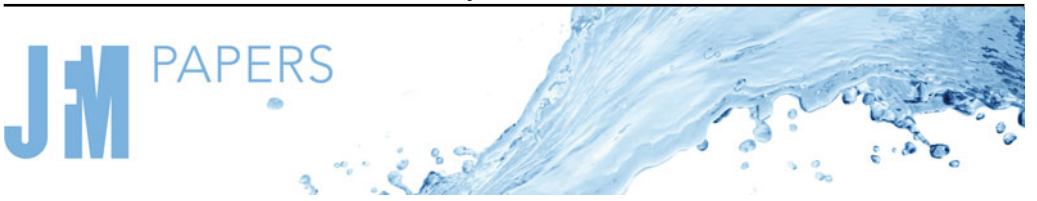

Lighthill's mechanism and vorticity cascade in the logarithmic layer of wall turbulence

Samvit Kumar[1], **Simon Toedtli**[2], **Tamer A. Zaki**[1,2] and **Gregory L. Eyink**[1,2]

[1]Department of Applied Mathematics & Statistics, Johns Hopkins University, Baltimore, MD 21218, USA

[2]Department of Mechanical Engineering, Johns Hopkins University, Baltimore, MD 21218, USA

Corresponding author: Samvit Kumar, skumar67@jhu.edu

(Received 21 March 2025; revised 27 August 2025; accepted 31 August 2025)

We investigate Lighthill's proposed turbulent mechanism for near-wall concentration of spanwise vorticity by calculating mean flows conditioned on motion away from or toward the wall in an (friction Reynolds number) $Re_\tau = 1000$ database of plane-parallel channel flow. Our results corroborate Lighthill's proposal throughout the entire logarithmic layer, but extended by counter-flows that help explain anti-correlation of vorticity transport by advection and by stretching/tilting. We present evidence also for Lighthill's hypothesis that the vorticity transport in the log layer is a 'cascade process' through a scale hierarchy of eddies, with intense competition between transport outward from and inward to the wall. Townsend's model of attached eddies of hairpin-vortex type accounts for half of the vorticity cascade, whereas we identify necklace type or 'shawl vortices' that envelop turbulent sweeps as supplying the other half.

Key words: vortex dynamics, turbulent boundary layers

1. Introduction

In a famous review of boundary layers, Lighthill (1963) suggested that turbulent flows possess a mechanism that systematically concentrates spanwise vorticity sharply against the wall, despite the strong 'eddy viscosity' effects that would be expected to diffuse such vorticity outward. He proposed that a tight correlation should exist, on the one hand, between motion toward the wall and vortex stretching/strengthening and, on the other hand, between motion away from the wall and vortex compression/weakening (see Lighthill 1963, § 3.3). Moreover, he argued that this mechanism should operate across the entire logarithmic layer and the correlated motions should constitute a turbulent 'cascade process':

'We may think of them as constantly bringing the major part of the vorticity in the layer close to the wall, while intensifying it by stretching and, doubtless, generating new vorticity at the surface; meanwhile, they relax the vortex lines which they permit to wander into the outer layer. Smaller-scale movements take over from these to bring vorticity still closer to the wall, and so on. Thus, . . . this cascade process has the additional effect in a turbulent boundary layer of bringing the fluctuations into closer and closer contact with the wall, while their vortex lines are more and more stretched'. – Lighthill (1963), p.99.

These ideas seem to have much in common with the attached eddy model (AEM) of Townsend (1976), a popular vortex-based structure model of turbulent boundary layers which has been substantially further investigated and developed (Woodcock & Marusic 2015; Marusic & Monty 2019). In this approach, the boundary layer is modelled as a scale-invariant hierarchy of 'attached eddies' often taken to be hairpin vortices similar to the structure visualised in figure 1(*a*). These eddies are assumed to have dimensions which scale with wall distance y and with a population size decreasing $\propto 1/y$, consistent with an inverse cascade in which hairpin vortices generated by a bursting process lift from the wall, grow in size and sequentially merge together.

There have been sporadic attempts to unify Lighthill's vorticity-based picture of turbulent boundary layers with the bursting phenomenon and the AEM (Gad-el Hak 1990). Using the standard assumptions in the AEM that the eddy-intensity function satisfies $I_{xy}(y^*) \sim -Qy^*$ for $y^* \ll 1$ and $I_{xy}(y^*) \to 0$ for $y^* \gtrsim 1$ (Townsend 1976; Woodcock & Marusic 2015), where Q is a numerical prefactor, Eyink (2008) showed that the ensemble-average nonlinear vorticity flux in the AEM for turbulent channel and pipe flow with friction velocity u_τ and outer length H (with v and w representing the wall-normal and spanwise velocities, ω_y and ω_z wall normal and streamwise vorticities, respectively) is (see Eyink 2008 for details)

$$\langle v\omega_z - w\omega_y \rangle \propto -\frac{Qu_\tau^2}{H}. \tag{1.1}$$

The AEM thus predicts the correct outward nonlinear flux of vorticity away from the wall at heights $y > y_p$, the location of peak Reynolds stress, consistent with some contemporary claims that the AEM applies only for that range of wall distances (Marusic & Monty 2019). The standard AEM, however, certainly does not explain the nonlinear vorticity transport flux toward the wall in the lower part of the log layer for $y < y_p$ (Eyink 2008, § III.B.2). The latter phenomenon was the main focus of Lighthill (1963) and its absence in the standard AEM suggests that a complement is needed. Recently, vorticity-based methods have provided some evidence in support of Lighthill's mechanism, first in a transitional boundary layer by a stochastic Lagrangian analysis (Wang, Eyink & Zaki 2022) and next in a fully developed turbulent channel flow, both by an Eulerian analysis of vorticity flux (Kumar, Meneveau & Eyink 2023) and also by Lagrangian analysis (Xiang, Eyink & Zaki 2025).

Here, we make a definitive advance by calculating conditional averages (Kim & Moin 1986; Adrian *et al.* 1989) of velocity fields and vorticity fluxes for positive or negative values of wall-normal velocity throughout the entire log layer. Our results for the conditional mean vorticity flux and the vortex lines of the conditional mean fields presented in detail below support the view that Lighthill's mechanism acts in the same manner throughout that entire range, with the conditional structures merely growing in scale with increasing distance of the conditioning point from the wall. As a preview of these results, we show in figure 1 the mean vortex structures and vortex lines conditioned at one height y_c. Details of the numerical methods are given in § 2.2. The results shown in figure 1(*a*) are conditioned on motion outward from the wall at the point $y_c^+ = 92.8$

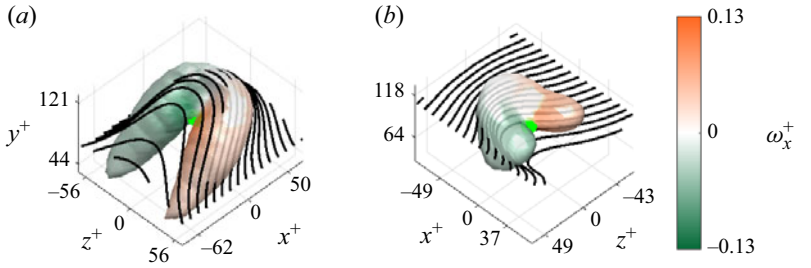

Figure 1. Conditional eddies visualised for $\lambda_2 = -0.9$, coloured by ω_x^+, along with vortex lines initiated at $y^+ = 60$ for (*a*) $v(y_c) > v_{rms}$ (click for three-dimensional version: https://www.cambridge.org/S002211202510654X/JFM-Notebooks/files/fig1/eddy_streamline_outflow_yplus_093.html) and at $y^+ = 108$ for (*b*) $v(y_c) < -v_{rms}$, (click for three-dimensional version: https://www.cambridge.org/S002211202510654X/JFM-Notebooks/files/fig1/eddy_streamline_inflow_yplus_093.html) with both conditions applied at $y_c^+ = 92.8$. A green dot marks the conditioning point.

inside the log layer. The vortex structure has the familiar form of a 'hairpin vortex', with an elevated spanwise head above the conditioning point and streamwise legs near the wall. On the other hand, the results shown in figure 1(*b*) for conditioning on motion inward to the wall at the same point inside the log layer appear quite distinct. The conditional structure appears as a broad necklace vortex, or 'shawl vortex', wrapped around the down-flowing fluid mass. We remark that these are similar to a smoothed version of the vortex structures visualised in Kumar *et al.* (2023) for a velocity field spectrally filtered to contribute only up-gradient nonlinear vorticity flux. Observations qualitatively similar to these will be presented below for conditioning points at every wall distance in the log layer. The vortex lines for our two conditions closely resemble those for the conditions QD2 and QD4 in the classic work of Kim & Moin (1986), except that they studied momentum transport whereas we focus on vorticity transport. For a more quantitative discussion, therefore, we must first recall the definition of Eulerian vorticity flux which is the basis of our work.

2. Methods of the present study

2.1. *Theoretical methods*

The analysis of the present work relies on the Eulerian vorticity-flux tensor originally introduced by Huggins (1971, 1994) (see also Eyink 2008; Terrington, Hourigan & Thompson 2021; Kumar *et al.* 2023; Kumar & Eyink 2024; Du & Zaki 2025) which for incompressible Navier–Stokes with viscosity ν, is

$$\Sigma_{ij} = u_i\omega_j - u_j\omega_i + \nu\left(\frac{\partial\omega_i}{\partial x_j} - \frac{\partial\omega_j}{\partial x_i}\right). \tag{2.1}$$

The above tensor describes the spatial flux of the jth component of vorticity in the ith coordinate direction, with its anti-symmetry arising from the fact that vortex lines cannot terminate in the fluid (Terrington *et al.* 2021). Thus, this tensor appears as a space-transport term in the local balance equations for the jth components of vorticity, $\partial_t\omega_j + \partial_i\Sigma_{ij} = 0$ for $j = 1, 2, 3$. The three terms in (2.1) have transparent physical meaning, with the first representing advective transport of vorticity, the second transport by stretching and tilting of vorticity and the third transport by viscous diffusion of vorticity.

The most important component of the vorticity flux for explanation of drag is Σ_{yz}, the flux of spanwise z-vorticity in the wall-normal y-direction (Kumar & Eyink 2024). It has been pointed out by many researchers (Taylor 1932; Huggins 1994; Klewicki *et al.* 2007;

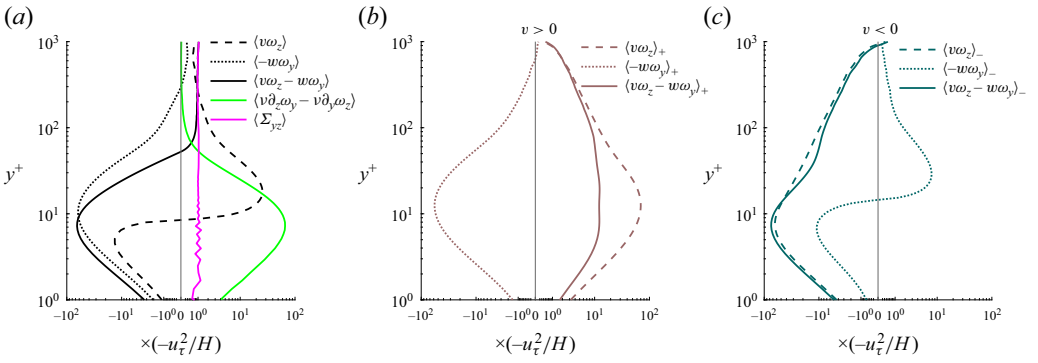

Figure 2. Profiles of the mean vorticity-flux contributions (a), averaged over time and wall-parallel planes, plotted as functions of wall distance. The vertical light grey line at zero flux is added to emphasise the signs of the various contributions. Conditional averages are plotted in (b) from points where turbulent flow is outward ($v' > 0$) and in (c) where it is inward ($v' < 0$), for the total nonlinear flux and its advective and stretching/tilting parts. The latter two are anti-correlated over the log layer, both for (b) inflow and (c) outflow.

Eyink 2008; Brown, Lee & Moser 2015; Kumar *et al.* 2023) that the mean value of this flux in statistically steady-state Poiseuille flow is exactly equal to the pressure gradient in the streamwise x-direction, and furthermore is constant in y for pipe and channel flows because of stationarity and conservation of vorticity (u_τ friction velocity, H channel half-width)

$$\langle \Sigma_{yz} \rangle = \langle v\omega_z - w\omega_y - \nu(\partial_y\omega_z - \partial_z\omega_y) \rangle = \partial_x \langle p \rangle = -u_\tau^2/H. \tag{2.2}$$

As stressed by Huggins (1994), (2.2) is a classical equivalent of the time-average relation of Josephson (1965) and Anderson (1966) for quantum superfluids, which relates drag to vortex motion. Here, we always mean Σ_{yz} whenever we refer to 'vorticity flux'.

In the prior work by Kumar *et al.* (2023), the constant-flux relation (2.2) was verified by numerical simulation data, together with the observations of Klewicki *et al.* (2007), Eyink (2008) and Brown *et al.* (2015) that $\langle v\omega_z - w\omega_y \rangle > 0$ for $y < y_p$ and $\langle v\omega_z - w\omega_y \rangle < 0$ for $y > y_p$, where y_p is the wall-distance location of the peak Reynolds stress; see figure 2(a), which reproduces figure 5 in Kumar *et al.* (2023) for the friction Reynolds number $Re_\tau = 1000$ channel-flow database where $y_p^+ = 52$. Since Lighthill (1963) had argued for strong correlation with the wall-normal velocity, Kumar *et al.* (2023) calculated also the average fluxes conditioned on $v > 0$ and $v < 0$. These conditional means are presented in figure 2(b,c), reorganising the data from figure 7 in Kumar *et al.* (2023). As shown, the net nonlinear vorticity flux is 'down-gradient' or away from the wall for $v > 0$ and 'up-gradient' or toward the wall for $v < 0$. As intuitively obvious, the mean advective flux contribution has these same signs, but intriguingly figure 2(b,c) shows that the mean stretching/tilting contribution has the opposite sign throughout the logarithmic layer. Kumar *et al.* (2023) presented a tentative explanation of this anti-correlation effect based on an assumed geometry of vortex lines and Lighthill's predicted flow behaviour: spanwise converging for $v > 0$ and spanwise diverging for $v < 0$. The main goal of the present work is to check Lighthill's picture in detail, and also the related explanation for anti-correlation, by calculating mean flow structures and their vortex lines conditioned on the wall-normal velocity at various points throughout the log layer.

2.2. *Numerical methods*

We employ direct numerical simulation data of channel flow at $Re_\tau = 1000$ from the Johns Hopkins Turbulence Database (see Li *et al.* 2008; Graham *et al.* 2016). We have used

y_c^+	No. of v_+ events	No. of v_- events	$x_w^+ \times z_w^+$
39	20 593	20 366	515 × 208
52	16 954	16 775	515 × 257
93	12 143	12 033	614 × 307
197	7925	7849	712 × 405
298	4660	4720	810 × 601

Table 1. Number of outflow and inflow events sampled at various wall-normal locations along with the streamwise (x_w) and spanwise (z_w) extent of the sampling window.

the database cut-out service to download time snapshots of data for the entire channel. Gradients in the spanwise and streamwise directions are then calculated spectrally by Fast Fourier Transform, and wall-normal gradients are calculated using seventh-order basis splines based on the collocation points of the original simulation (Graham *et al.* 2016). All statistics are thereafter calculated by averaging over wall-parallel planes in the x and z directions of homogeneity, as well as over 10 time snapshots. Reflected results from the top half of the channel are included to double the sample size of our averages.

Our conditional averaging was designed to select points with a local maximum of wall-normal velocity magnitude $|v(\boldsymbol{x})|$ exceeding some threshold αv_{rms}. We have checked that our results do not depend very sensitively upon the choice of α and we present results here only for $\alpha = 1$. We may argue for the reasonableness of this choice by noting that, for both signs $\pm$ of v and independent of y, the set of points with $|v| > v_{rms}$ constitute 10 % of the area of the wall-parallel plane at that y-level but contribute approximately 60 % of the total vorticity flux for that sign of v, as plotted in figure 2(*b*,*c*); see Appendix A. To make certain that the events in the conditional ensemble are distinct, we set streamwise (x_w) and spanwise (z_w) extents of the sampling window for each event. For each sign $\pm$ of v and each y-level, we then performed sequentially the following steps: (i) identify the point with largest magnitude of $|v|$ (and above the root mean square v_{rms}) in the wall-parallel plane, (ii) add the sample of size $x_w \times z_w$ centred at that point, (iii) remove from the plane the doubled $2x_w \times 2z_w$ rectangle centred at the point in order to prevent overlap, (iv) find the next point with largest magnitude of $|v|$ (and above v_{rms}) in the remaining portion of the wall-parallel plane and so forth. The size of the sampling window at each y-level was selected by calculating approximate conditional averages with a linear estimator (Adrian *et al.* 1989) and determining the smallest rectangle to contain the conditional eddy visualised by the λ_2-criterion at a low threshold.

The sizes of the sampling windows and the number of events in the conditional ensembles for each sign $\pm$ and for five values of $y = y_c$ distributed through the log layer are given in table 1. For decreasing y_c, the sizes of the events decrease, as measured by the areas $x_w \times z_w$, while the total number of events increase. In fact, as an *a posteriori* justification of our sampling procedure, we note that the percentage of the total area occupied both by the outflow (v_+) events and by the inflow (v_-) events is approximately 47 % for each sign, independent of y_c. This y-independence of the area fraction is expected of the 'representative eddies' in the AEM, but notice that such independence holds here for the v_- events or 'sweeps' as well as for the v_+-events or 'ejections'. In fact, the events in our two conditional ensembles cover together nearly the entire area of the wall-parallel plane at each y. Note that for all y-levels except the largest there are slightly more v_+ events than v_- events at the same threshold, reflecting the well-known asymmetry in strengths of 'ejections' versus 'sweeps' (Willmarth & Lu 1972; Kim & Moin 1986; Hutchins *et al.* 2011; Lozano-Durán *et al.* 2012).

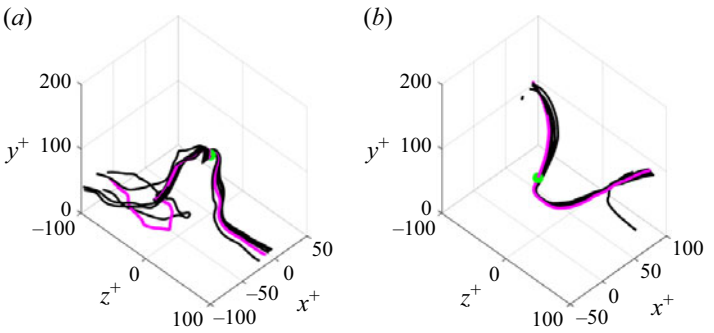

Figure 3. Instantaneous vortex lines for (*a*) outflow event (*b*) inflow event, both in the vicinity of a local maximum of the wall-normal velocity at $y^+ = 92.8$. The unique vortex line passing through the conditioning point is marked in magenta.

To provide some intuition about the events selected by our sampling procedure, we plot in figure 3 one event in the v_+ ensemble and another in the v_- ensemble. To visualise these events, we have followed Kim & Moin (1986) in drawing the unique vortex line passing through the conditioning point and also nearby vortex lines. The resulting bundle of vortex lines for the outflow event in figure 3(*a*) is easily recognisable as a 'hairpin vortex', while the bundle for the inflow event in figure 3(*b*) is instead an 'inverted hairpin'. These two events are for the same wall distance $y_c^+ = 92.8$ as the mean structures plotted in figure 1, where the means are obtained by averaging over the entire conditional ensembles, hereafter denoted as $\langle\cdot\rangle_{+,y_c}$ and $\langle\cdot\rangle_{-,y_c}$, respectively. (We omit y_c, if it is clear in context.) For more such events, see Appendix B. The two events plotted in figure 3 have the largest magnitudes of $|v(\boldsymbol{x})|$ for the given time, sign and y-level.

3. Results of conditional averaging

We present our results first for averages conditioned on outflow (§ 3.1) and then on inflow (§ 3.2). The log layer in the $Re_\tau = 1000$ database extends over the range $30 \lesssim y^+ \lesssim 300$ and we present results in the first two sections for a single height $y_c^+ = 92.8$, roughly at the geometric mean of the log layer. Finally, we consider (§ 3.3) the variation of our numerical results with wall distance y^+ and the evidence for a scale hierarchy.

3.1. *Outflow from the wall*

In figure 4 we plot the contributions to the mean vorticity flux and the mean flow for the conditional average $\langle\cdot\rangle_{+,y_c}$ at $y_c^+ = 92.8$. The first panel figure 4(*a*) plots the mean advective flux under this condition, which is straightforwardly down-gradient throughout most of the domain. There is only a very narrow layer at $y^+ \lesssim 10$ where the convective flux contribution is up-gradient. The latter effect was explained in Kumar *et al.* (2023) by the correlation between weakened spanwise vorticity and upward motion in this near-wall region. On the other hand, the second panel, figure 4(*b*), which plots the mean stretching/tilting contribution, shows strong up-gradient flux below the conditioning point, especially near the wall, and a weaker down-gradient flux in the region above the conditioning point. The main goal of this subsection is to explain these observations.

The most significant clues to the correct explanation are in the remaining panels. Figure 4(*c*) plots in the yz-plane of the conditioning point the vortex lines of the mean flow. These show the 'hairpin' structure of vortex lines already evidenced by the three-dimensional (3-D) plot in figure 1(*a*). Furthermore, figure 4(*d*) shows that the conditional flow corresponds to a large-scale 'ejection' between a pair of counter-rotating streamwise

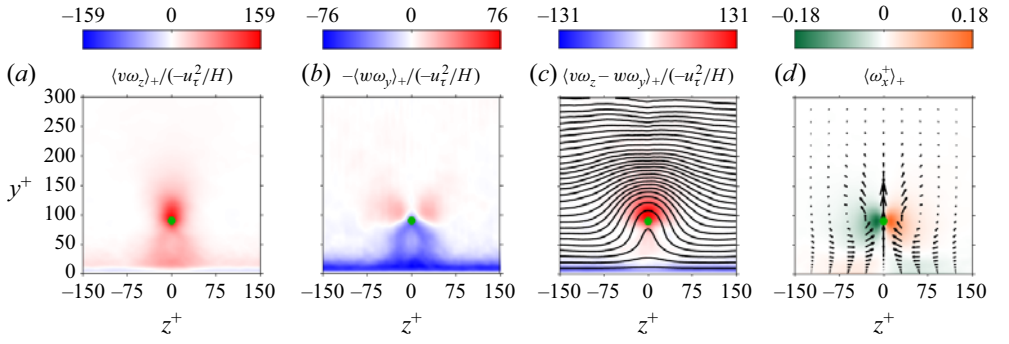

Figure 4. Conditional mean fields in the plane of the conditioning point for the outflow event at $y_c^+ = 92.8$, coloured by (*a*) flux due to the convective term, (*b*) flux from the stretching/tilting term, (*c*) total nonlinear flux, (*d*) streamwise vorticity. Also depicted are (*c*) vortex lines and (*d*) quivers showing in-plane velocity. A green dot marks the conditioning point.

vortices. Below these vortices are oppositely oriented streamwise rollers, illustrating Lighthill's remark in the opening quotation of this paper about 'generating new vorticity at the surface' due to the stick boundary condition at the wall. See figure II.19 in Lighthill (1963).

These characteristics were exactly those predicted by Lighthill (1963) to explain the up-gradient flux due to weakening of vortex lines and were also the ingredients of the control-volume argument by Kumar *et al.* (2023) to explain the anti-correlation between advection and stretching contributions during outflow. We repeat this argument in figure 5(*a*), with attention on the bottom line, taken as representative of all lines below the conditioning point. Because of the spanwise converging flow, the product $-w\omega_y > 0$ gives an up-gradient transport into the grey-shaded control volume, representing the loss of spanwise vorticity of the lifted vortex line. This is precisely Lighthill's mechanism, based on converging flow that compresses and weakens the upward-moving vortex lines. Note from figure 4(*d*) that the mean flow is converging all the way up to the conditioning point. Thus, not only does the conditional mean flow support Lighthill's mechanism near the wall, but it also shows that Lighthill's mechanism can explain the observed anti-correlation at the conditioning point and in a region below it.

Note, however, that the flow above the conditioning point is instead diverging, because of the counter-flow required by incompressibility but neglected in the considerations of Lighthill (1963). His reasoning would suggest that rising vortex lines in this region are being stretched and strengthened. This effect is associated with the product $-w\omega_y < 0$ for the upper vortex line above the conditioning point in figure 5(*b*), which corresponds to down-gradient flux out of the top surface of the grey-shaded control volume and into the lifted vortex head. In fact, down-gradient flux from stretching/tilting is indeed observed in this region in figure 4(*b*).

Finally, together with the vortex lines in figure 4(*c*), we have plotted the conditional mean nonlinear vorticity flux from both advection and stretching/tilting. This total nonlinear flux is down-gradient everywhere except near the wall, because the advection term is generally stronger than the stretching term. However, Lighthill's mechanism dominates near the wall, producing net up-gradient vorticity flux toward the wall.

3.2. *Inflow to the wall*

In figure 6 we plot the analogous contributions to the mean vorticity flux and the mean flow for the conditional average $\langle\cdot\rangle_{-,y_c}$ at $y_c^+ = 92.8$. The advective flux plotted in figure 6(*a*)

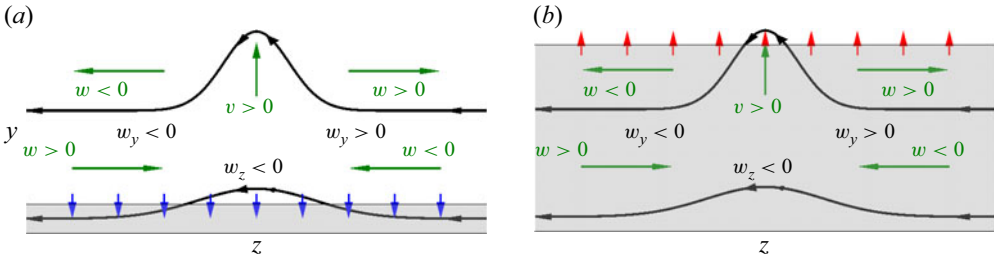

Figure 5. Control-volume analysis of outflow away from the wall illustrating the stretching contribution to spanwise vorticity balance for (*a*) Lighthill region, (*b*) counter-flow region. Black lines with arrows represent vortex lines and green arrows mark the directions of local velocity components. Blue arrows in (*a*) at the boundary of the relevant control volume, shaded grey, represent up-gradient flux from the stretching–tilting term into the volume, while red arrows in (*b*) represent down-gradient flux out of the volume.

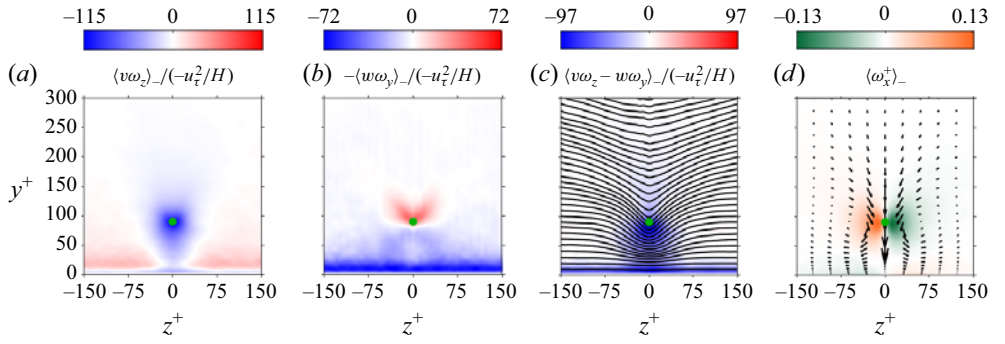

Figure 6. Conditional mean fields in the plane of the conditioning point for the inflow event at $y_c^+ = 92.8$, coloured by (*a*) flux due to the convective term, (*b*) flux from the stretching/tilting term, (*c*) total nonlinear flux, (*c*) streamwise vorticity. Also depicted are (*c*) vortex lines and (*d*) quivers showing in-plane velocity. A green dot marks the conditioning point.

is again straightforwardly up-gradient near the conditioning point where the mean flow is toward the wall, but down-gradient below and to the sides. The latter sign can be explained as a counter-flow effect: see the flow vectors in figure 6(*d*) directed away from the wall in this region. The up-gradient advective flux in the layer $y^+ \lesssim 10$ was already observed in Kumar *et al.* (2023) and explained there by the correlation between strengthened spanwise vorticity and downward motion in the very near-wall region. The second panel, figure 6(*b*), plots the mean stretching/tilting contribution and shows down-gradient flux in a small region at and just above the conditioning point. On the other hand, close to the wall the stretching contribution is strongly up-gradient. In this subsection we develop an explanation of these various observations.

As before, the most significant pieces of information are in the remaining panels of figure 6. The vortex lines of the mean flow plotted in figure 6(*c*) over the yz-plane of the conditioning point and plotted also for three dimensions in figure 1(*b*) have the form of 'inverted hairpins'. Furthermore, figure 6(*d*) shows that the conditional flow corresponds to a large-scale 'sweep' between a pair of counter-rotating streamwise vortices, opposite in orientation to the pair in figure 4(*d*), and again with induced streamwise rollers of the opposite sign near the wall. These characteristics are precisely those predicted by Lighthill (1963) for in-flow to the wall, with a spanwise diverging flow beneath the conditioning point. To understand the up-gradient transport of the stretching term in that region, we can use a control-volume analysis which assumes a field-line geometry like that illustrated in

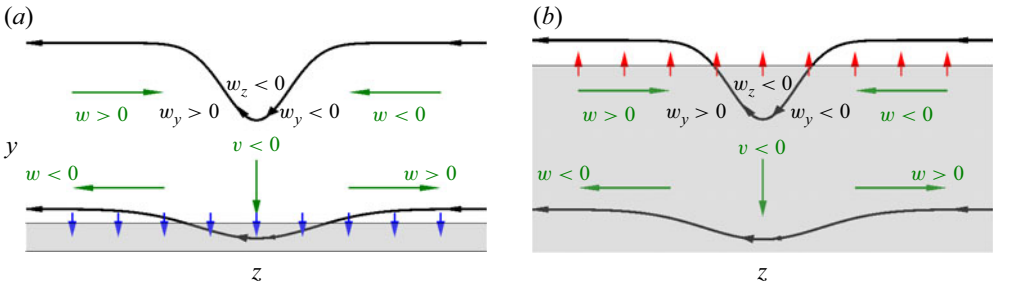

Figure 7. Control-volume analysis of inflow towards the wall illustrating the stretching contribution to spanwise vorticity balance for (*a*) Lighthill region, (*b*) counter-flow region. Conventions for lines, arrows and their colours are the same as in figure 5.

figures 1(*b*) and 6(*c*); see the bottom line sketched in figure 7(*a*). Because of the spanwise diverging flow, the product $-w\omega_y > 0$ gives an up-gradient transport into the grey-shaded control volume, representing the gain of spanwise vorticity of the vortex line. This is exactly Lighthill's mechanism, based on diverging flow that stretches and strengthens the downward-moving vortex line.

As with the out-flow case, however, a recirculation appears that was not considered by Lighthill and that leads now to a converging flow above the conditioning point; see figure 6(*d*). Lighthill's reasoning would suggest here that the down-moving vortex lines in this region are compressed and weakened. This effect is associated with the product $-w\omega_y < 0$ for the upper vortex line above the conditioning point in figure 7(*b*), which corresponds to down-gradient flux out of the top surface of the grey-shaded control volume and weakening of the vortex line. This argument thus suggests that the anti-correlation between advective and stretching contributions is in fact due to the counter-flow in the case that $v' < 0$ and the control-volume picture in figure 7(*b*) corrects that of Kumar *et al.* (2023), which erroneously posited an upward-bent hairpin-type line geometry.

We plot also in figure 6(*c*) the conditional mean nonlinear vorticity flux from both advection and stretching/tilting, together with the vortex lines. This total nonlinear flux is up-gradient everywhere, because the advection term is stronger than the stretching term near the conditioning point. However, Lighthill's mechanism again dominates near the wall, so that the net flux is likewise up-gradient close to the wall. As already emphasised by Lighthill (1963), both outflow and inflow act to concentrate vorticity near the wall, the first through weakening and the second through strengthening of the advected vorticity.

Our explanation of the conditionally averaged vorticity fluxes $\langle v\omega_z\rangle_\pm$, $-\langle w\omega_y\rangle_\pm$ based on the conditionally averaged fields is *a priori* valid only for the fluxes $\langle v\rangle_\pm\langle\omega_z\rangle_\pm$, $-\langle w\rangle_\pm\langle\omega_y\rangle_\pm$ of the conditional eddies themselves. The success of this explanation requires that correlations of the two fluctuating factors must be rather small in the conditional ensembles. We have directly verified the small size of the Pearson correlation coefficients (see Appendix C), but a complete physical justification remains open. A possible explanation is that the velocities v, w are mainly large-scale quantities while the vorticities ω_z, ω_y are mainly small-scale quantities and fluctuations of the two sets of variables are thus naturally uncorrelated due to scale separation (Tennekes & Lumley 1972, § 8.2). However, statistical correlations between these variables are obviously required for turbulent nonlinear transport of vorticity. One may infer from the small Pearson coefficients observed in the conditional ensembles that these correlations are mainly linked to the direction of the wall-normal velocity, as intuited by Lighthill. This fact provides strong *a posteriori* justification for our procedure of conditioning on the wall-normal velocity.

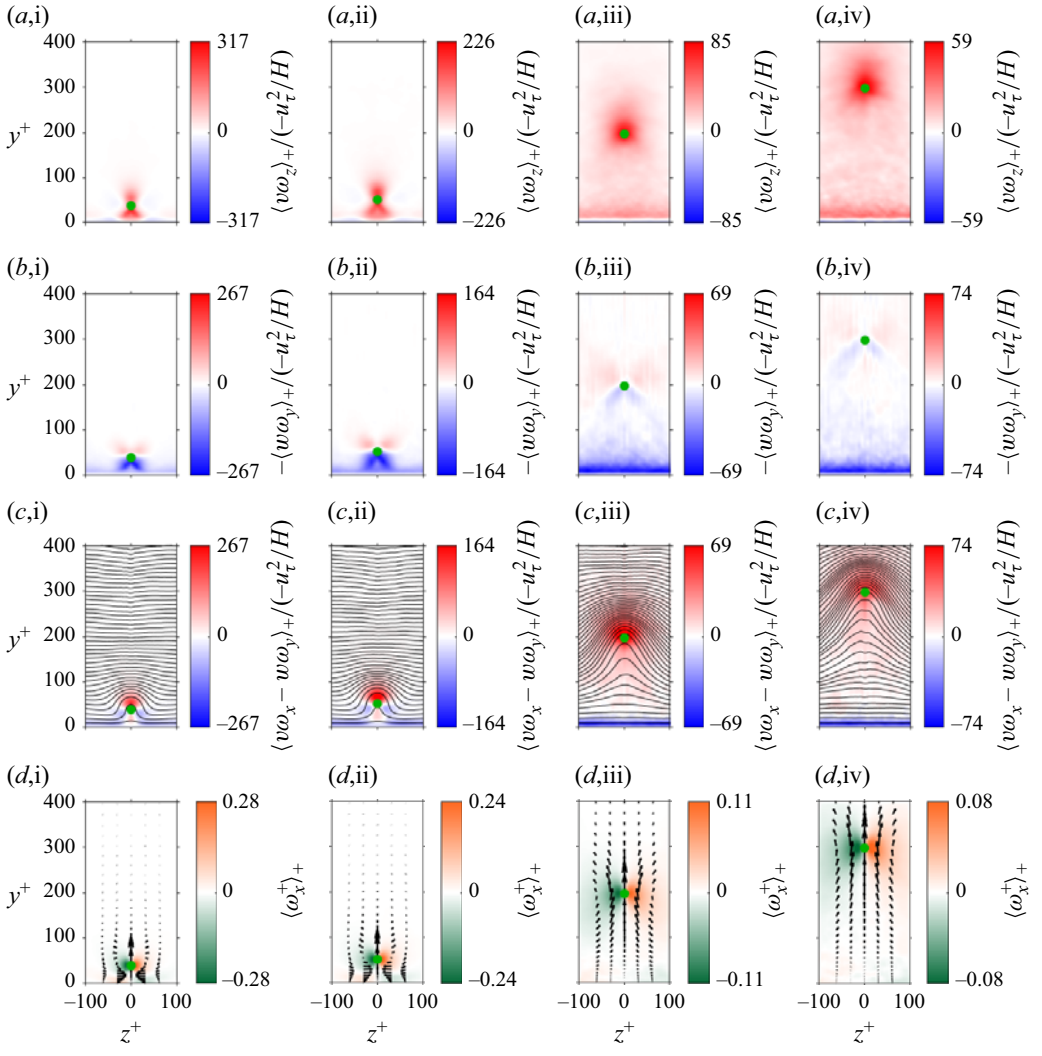

Figure 8. Conditional fields for outflow events at (*a–d*,i) $y_c^+ = 39$, (*a–d*,ii) $y_c^+ = 52$, (*a–d*,iii) $y_c^+ = 197$, (*a–d*,iv) $y_c^+ = 298$, coloured by (*a*,i–iv) flux due to the convective term, (*b*,i–iv) flux from the stretching/tilting term, (*c*,i–iv) nonlinear flux and vortex lines in black, (*d*,i–iv) streamwise vorticity and in-plane velocity as quivers. Green dots mark conditioning points.

3.3. *Scaling with wall distance*

The results presented previously for conditioning point $y_c^+ = 92.8$ hold for all points within the log layer. We show in figure 8 at four y_c-values in the log layer results for outflow analogous to those in figure 4 for $y_c^+ = 92.8$, and likewise in figure 9 at the same four y_c-value results for inflow analogous to those in figure 6. The essential features are the same for all y_c as for $y_c^+ = 92.8$, with each panel of figure 8 showing an ejection between a pair of counter-rotating streamwise vortices and each panel of figure 9 a sweep between a counter-rotating vortex pair of the opposite orientation. The primary change with increasing y_c is the increased scale of the conditional mean events, along with decreasing magnitude of the mean fluxes. Only minor qualitative changes with y_c appear, such as a small region of down-gradient transport near the wall in the total vorticity flux in

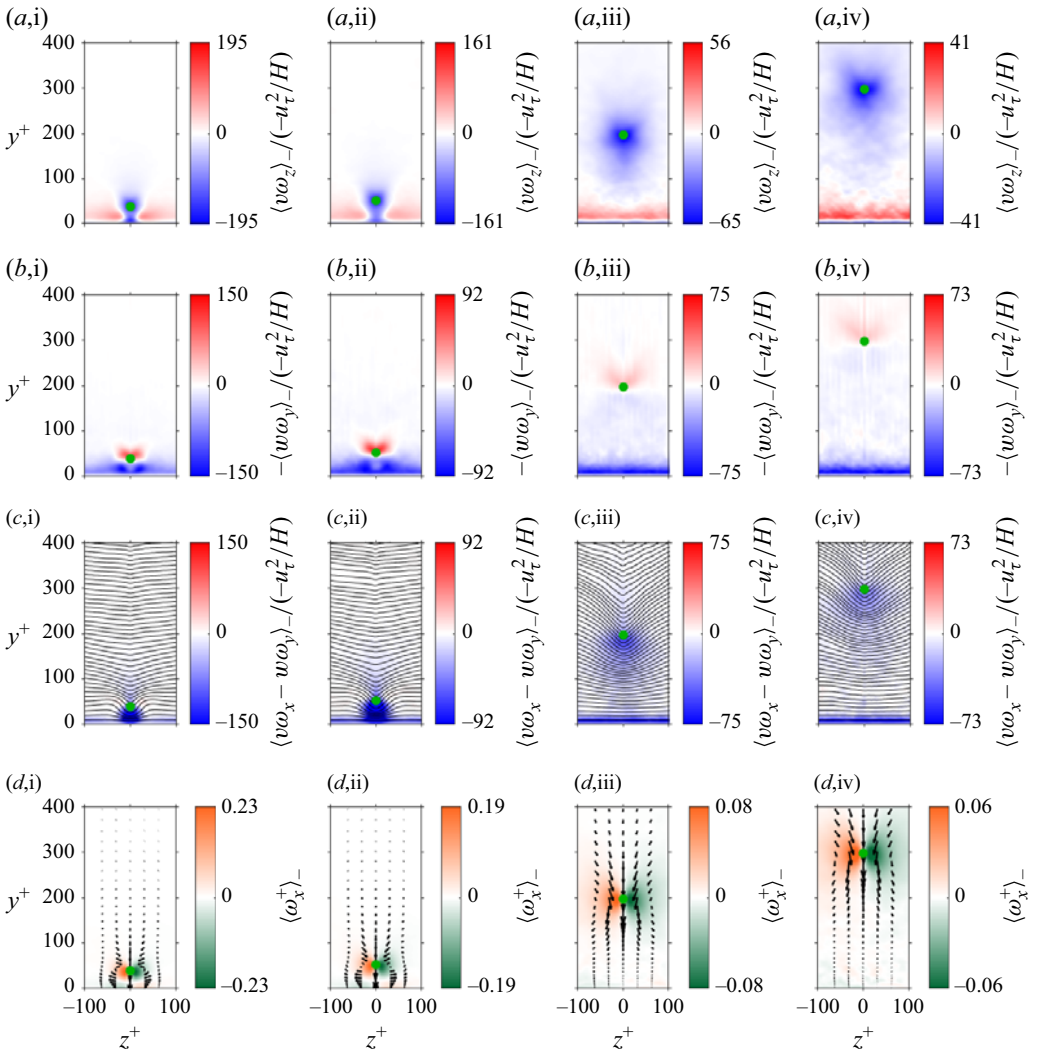

Figure 9. Conditional fields for inflow events at (*a–d*,i) $y_c^+ = 39$, (*a–d*,ii) $y_c^+ = 52$, (*a–d*,iii) $y_c^+ = 197$, (*a–d*,iv) $y_c^+ = 298$, coloured by (*a*,i–iv) flux due to the convective term, (*b*,i–iv) flux from the stretching/tilting term, (*c*,i–iv) nonlinear flux and vortex lines in black, (*d*,i–iv) streamwise vorticity and in-plane velocity as quivers. Green dots mark conditioning points.

figure 8 for outflows at $y_c^+ \lesssim 52$ and a single connected region of down-gradient transport near the wall for the advective flux in figure 9 for inflows at $y_c^+ \gtrsim 197$. Except for these small differences, the plots are nearly the same for all values of y_c. These results support the conjecture of Lighthill (1963) that vorticity transport through the log layer is a 'cascade process' sustained by a scale hierarchy of vortex structures.

Additional evidence for scale similarity is provided in figure 10, which shows conditional mean eddies for outflow and for inflow at various conditioning points with heights y_c selected throughout the log layer, analogous to the structures plotted in figure 1 for $y_c^+ = 92.8$. These eddies are defined by the λ_2-criterion for the conditional mean fields with a threshold $\lambda_2 = -6u_\tau^2/y_c^2$ that is scaled with u_τ and y_c. Note that the structures are not strongly sensitive to the prefactor 6 in the λ_2 threshold and that 3-D versions of

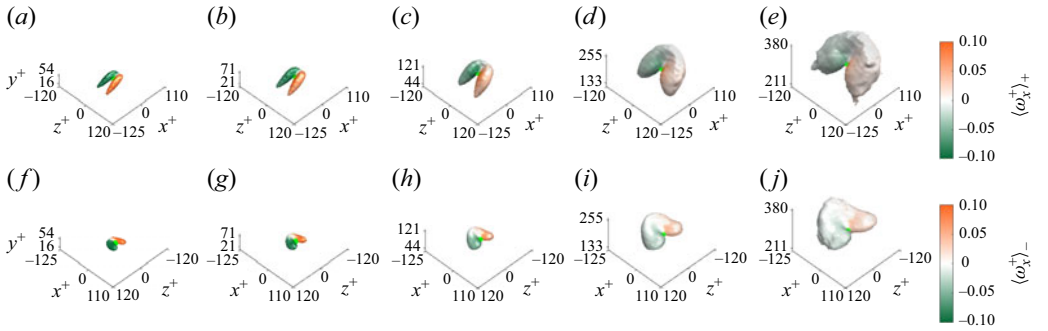

Figure 10. Outflow eddies (top), inflow eddies (bottom) are illustrated for the conditioning point at (a,f) $y_c^+ = 39$, (b,g) $y_c^+ = 52$, (c,h) $y_c^+ = 92.8$, (d,i) $y_c^+ = 197$, (e,j) $y^+ = 298$. The isosurfaces are shown at $\lambda_2 = -6u_\tau^2/y_c^2$. Three-dimensional versions of the eddies sketched in this figure, as well as corresponding streamlines for the outflow event, are available to view by clicking on (a), (b), (c), (d), (e), and for the inflow event at (f), (g), (h), (i), (j). The code to generate outflow eddies is available in figure 10$(a–e)$ code here: https://www.cambridge.org/S0022112025106654X/JFM-Notebooks/files/fig10/plot_outflow_eddies_streamlines.ipynb and to generate inflow eddies is available in figure 10$(f–j)$ code here: https://www.cambridge.org/S0022112025106654X/JFM-Notebooks/files/fig10/plot_inflow_eddies_streamlines.ipynb.

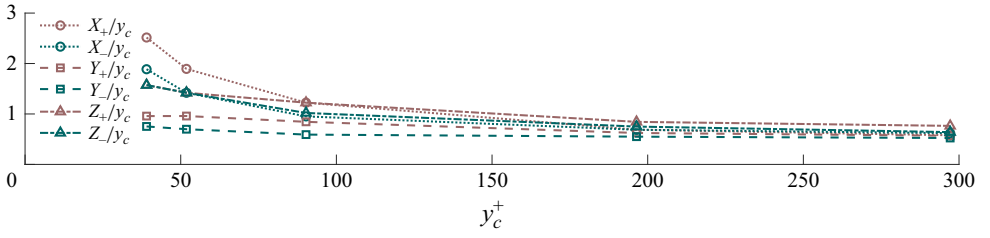

Figure 11. Streamwise (X_+, X_-), wall-normal (Y_+, Y_-) and spanwise (Z_+, Z_-) sizes of outflow and inflow conditional eddies scaled by the wall-normal location of the conditioning point.

all images are available via JFM Notebooks through links provided in the figure caption. The plots suggest that the conditional eddies change with increasing y_c chiefly through their streamwise extents decreasing with respect to their spanwise and wall-normal extents, while the latter scale linearly with y_c. These observations can be quantified by calculating the side lengths X, Y, Z for bounding boxes of the conditional eddies, which are plotted in figure 11 rescaled by y_c. As observed for both outflow (v_+) and inflow (v_-), the quantities $Y^\pm/y_c$ and $Z^\pm/y_c$ are nearly constant while streamwise size $X^\pm/y_c$ shows some decrease in value. Note also that the extents of outflow eddies are larger than inflow eddies, in part due to the stronger intensity of outflow events.

The difference in vorticity transport contributions between 'hairpins' and 'shawls' can be further emphasised by plotting as functions of y the conditional mean vorticity flux $\langle v\omega_z - w\omega_y\rangle_{\pm,y_c}$ for both signs $\pm$ of wall-normal velocity and for various values of y_c in the log layer; see figure 12. Most obviously, the flux contribution at the conditioning point $y = y_c$ of the v_+ eddies is always down-gradient, whereas the contribution of the v_- eddies at point $y = y_c$ is always up-gradient. Another important lesson to draw from the flux distributions in figure 12 is the locality of the vorticity transport in vertical height, with eddies at wall distance y_c contributing to vorticity flux only at distances $y \sim y_c$. In fact, for all values of y_c and both signs $\pm$, the mean vorticity transport arising from the conditional eddy appears only in the scale range $0.4 \lesssim y/y_c \lesssim 1.4$ and with a narrower range for

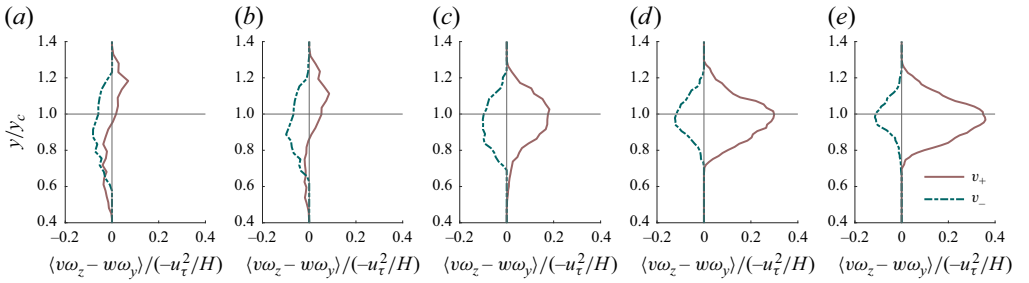

Figure 12. Flux contributions from conditional outflow and inflow eddies, for the conditioning point at (*a*) $y_c^+ = 39$, (*b*) $y_c^+ = 52$, (*c*) $y_c^+ = 92.8$, (*d*) $y_c^+ = 197$, (*e*) $y^+ = 298$.

larger y_c. This result is complementary to the locality in spanwise length observed by Kumar *et al.* (2023), whose plots of vorticity-flux cospectra in their figures 8 and 11 showed that down-gradient vorticity across height y is contributed on average by eddies with spanwise wavelengths λ_z in the range $0.4 \lesssim \lambda_z/y \lesssim 3$ while up-gradient vorticity across y is contributed on average by eddies with λ_z in the range $3 \lesssim \lambda_z/y \lesssim 40$. These two forms of locality are presumably closely connected, since our figure 11 shows that all three dimensions of the conditional mean eddies scale with y_c. The observation in Kumar *et al.* (2023) that up-gradient transport at wall distance y arises from eddies of larger scale while down-gradient transport arises from eddies of smaller scale is also suggested by our figure 12, since (at least for $y_c^+ \lesssim 93$) the peak of the up-gradient transport from v_- eddies occurs at $y < y_c$ and the peak of the down-gradient transport from v_+ eddies occurs at $y > y_c$. These various observations *in toto* lend support to Lighthill's conjecture that vorticity transport in wall-bounded turbulence occurs via a stepwise cascade through a hierarchy of eddies.

3.4. *Are sweeps and ejections really independent?*

Despite the differences documented above, comparison of the inflow and outflow structures in figure 10 might lead one to question whether these two conditional mean eddies exist as distinct entities. Instead, the logarithmic layer at every wall distance may be imagined to consist of a sequence of streamwise vortices with alternating orientations, and the decision to pair these into 'hairpins' and 'shawls' would then be an arbitrary choice. It seems clear by continuity of the flow that outflows and inflows cannot be distributed independently but instead must appear one after another in turn, along a spanwise direction. In fact, this sort of arrangement corresponds exactly to the sketch in figure II.22 of Lighthill (1963). Similarly in the plot of vortex lines in figure 3 for individual flow realisations, one might imagine that the hairpin and inverted hairpin are two pieces of a long vortex line undulating up and down in the spanwise direction and just shifted by half a phase.

To address these questions, we have carried out an extensive study of the distribution of inflow and outflow events identified for conditional averaging, with details given in Appendix D. (We thank an anonymous referee for suggesting this analysis.) Given any sweep or ejection event, we located the mean position of the neighbouring reverse flow event by looking at the autocorrelation function of the wall-normal velocity, in the same wall-normal plane. At each wall height, we observe a clear negative minimum of the auto-correlation at spanwise distance of $\sin 1.3y$, which we take as the average distance to the neighbouring reverse flow event. This seems a reasonable estimate also based on the conditional mean structures plotted in figure 10 and the individual realisations

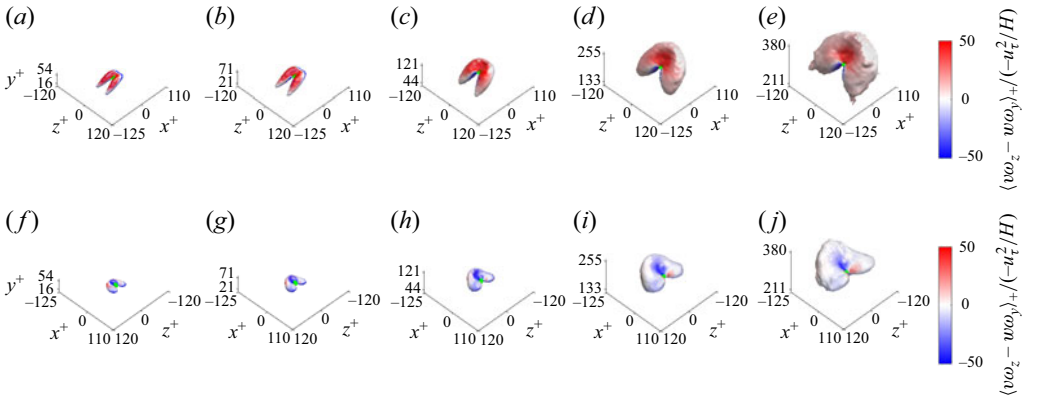

Figure 13. Outflow eddies (top), inflow eddies (bottom) are illustrated for the conditioning point at (a,f) $y_c^+ = 39$, (b,g) $y_c^+ = 52$, (c,h) $y_c^+ = 92.8$, (d,i) $y_c^+ = 197$, (e,j) $y^+ = 298$. The isosurfaces are shown at $\lambda_2 = -6u_\tau^2/y_c^2$ and are coloured by the associated nonlinear vorticity flux. Three-dimensional versions of the eddies sketched in this figure, as well as corresponding streamlines for the outflow event, are available to view by clicking on (*a*), (*b*), (*c*), (*d*), (*e*), and for the inflow event at (*f*), (*g*), (*h*), (*i*), (*j*). The code to generate outflow eddies is available in figure 13(*a–e*) code here: https://www.cambridge.org/S002211202510654X/JFM-Notebooks/files/fig13/plot_outflow_flux_eddies.ipynb and to generate inflow eddies is available in figure 13(*f–j*) code here: https://www.cambridge.org/S002211202510654X/JFM-Notebooks/files/fig13/plot_inflow_flux_eddies.ipynb.

plotted in figure 3 (see also figures 19 and 20). However, these neighbouring reverse events might not be sufficiently strong to satisfy the criterion imposed in our conditional ensemble. Thus, for each strong outflow event or ejection considered in the conditional average, we find the nearest strong inflow event or sweep on the same wall-parallel plane satisfying $|v| > v_{rms}$. We then find the displacement vector $\boldsymbol{d}$ between them. We consider displacement vectors $\boldsymbol{d}$ that make an angle $|\theta| < (\pi/4)$ with the z-axis and label these sweep events as possible 'spanwise shifts' of the ejection event. In fact, we find that these nearest sweep events are either much further away than $1.3y$ or else are displaced mainly streamwise, i.e. make an angle $|\theta| > (\pi/4)$. At increasing wall-normal distances in the log layer, only 9 %–26 % sweep events are shifts of ejection events defined in this way. This result implies that, although a spanwise phase shift from a strong outflow event may lead to an inflow event, the strength of this inflow event is usually not enough to merit inclusion in the conditional average, and *vice versa*. Strong outflow and strong inflow events tend not to be phase shifts of each other, but instead perceptibly different events.

In addition, the conditional eddies for outflows and inflows are distinct in several respects. For example, the 'hairpins' are more streamwise extended (see figure 11 for a quantification of this observation) and seem also more clearly 'wall attached', whereas the 'shawls' are streamwise shorter and appear detached. Even clearer differences appear in their contributions to vorticity transport. This becomes apparent in figure 13 where the conditional mean eddies are coloured instead by nonlinear vorticity flux. 'Hairpins' and 'shawls' both contain vorticity flux directed away from and toward the wall, but the distributions are distinctly different. For 'hairpins' the dominant flux is outward/down-gradient and appears on the upper half of the vortex, whereas weaker inward/up-gradient flux appears on the underside facing the wall. For 'shawls' the distribution is different, with the dominant inward/up-gradient flux appearing on top and immediately below, with weaker outward/down-gradient flux further underneath. The most distinctive and important difference is that the arch of spanwise vorticity in 'hairpins' is moving outward and contributes down-gradient vorticity flux, while the arch of spanwise vorticity in

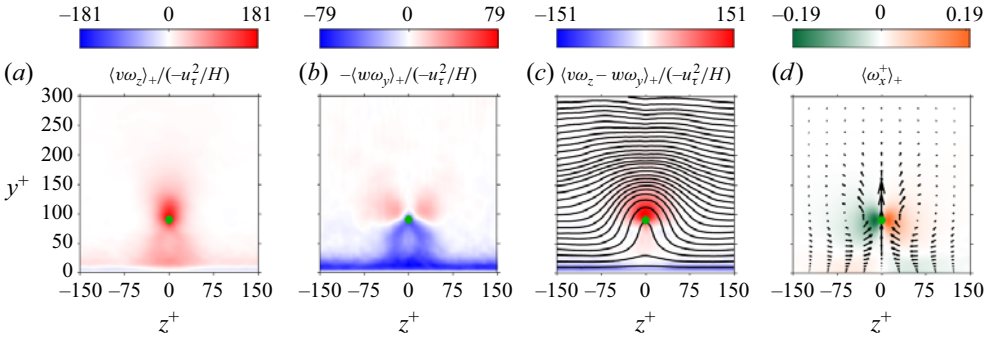

Figure 14. Conditional mean fields in the plane of the conditioning point for the outflow event $v > 2v_{rms}$ at $y_c^+ = 92.8$, coloured by (*a*) flux due to the convective term, (*b*) flux from the stretching/tilting term, (*c*) total nonlinear flux, (*d*) streamwise vorticity. Also depicted are (*c*) vortex lines and (*d*) quivers showing in-plane velocity. A green dot marks the conditioning point.

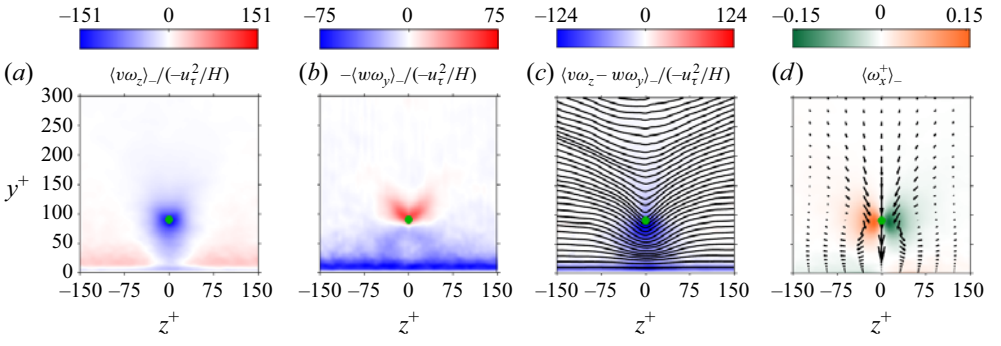

Figure 15. Conditional mean fields in the plane of the conditioning point for the inflow event $v < -2v_{rms}$ at $y_c^+ = 92.8$, coloured by (*a*) flux due to the convective term, (*b*) flux from the stretching/tilting term, (*c*) total nonlinear flux, (*d*) streamwise vorticity. Also depicted are (*c*) vortex lines and (*d*) quivers showing in-plane velocity. A green dot marks the conditioning point.

'shawls' is moving inward and contributes up-gradient vorticity flux. In fact, there is a striking similarity to the coherent structures observed by Kumar *et al.* (2023) in filtered fields, designed to decompose the flow into two orthogonal components contributing 'down-gradient' and 'up-gradient' transport. Figure 13 in Kumar *et al.* (2023) for the high-pass filtered field shows a forest of 'hairpins' with the same bipolar flux distribution as in the upper row of figure 13 and net 'down-gradient' transport. On the other hand, figure 15 in Kumar *et al.* (2023) for the low-pass filtered field shows an assembly of 'shawls' or 'pancakes' with the bipolar flux distribution as in the bottom row of figure 13 and net 'up-gradient' transport. The suggestive similarities between the structures revealed by conditional averaging and by spectral filtering remain to be fully understood.

Further evidence that 'ejections' and 'sweeps' are not just phase shifts of each other is provided by the distribution of the nonlinear vorticity flux in individual realisation of the two conditional ensembles, which are exhibited as colour plots in figures 19 and 20 in Appendix B. As suggested by the conditional mean structures plotted in figure 13, ejection events tend to have strong down-gradient flux just above the conditioning point while sweeps tend instead to have strong up-gradient flux just below that point. The neighbouring reverse flow events are usually weaker and do not have these characteristics. These features are most evident nearer the wall where the individual realisations are more coherent, but

remain as a statistical tendency at all wall distances. These differences in vorticity-flux distributions for individual realisations of the two conditional ensembles give additional support to the premise that they represent different types of events, which are not just spanwise phase shifts of each other.

4. Conclusions

The mechanism proposed by Lighthill (1963) for concentration of spanwise vorticity at solid walls in a turbulent boundary layer involves a strong correlation between vortex stretching/relaxation and fluctuating velocities toward/away from the wall. The method of conditional averaging (Kim & Moin 1986; Adrian *et al.* 1989) is designed to reveal such correlations and, applied here to a database of high-Re_τ turbulent channel flow, it provides extensive evidence corroborating the validity of Lighthill's mechanism throughout the logarithmic layer. We have elaborated this picture by observing, in addition to the near-wall motions postulated by Lighthill (1963), also returning counter-flows away from the wall, which help to explain, among other things, the anti-correlation between advective and stretching fluxes observed by Kumar *et al.* (2023). The net vorticity transport in the turbulent boundary layer is exposed as an intense rivalry between fluxes up-gradient toward the wall and down-gradient away from the wall, with the competition just narrowly won by the latter. Our results further support by an array of evidence Lighthill's conjecture that this vorticity dynamics is a cascade process proceeding through a hierarchy of turbulent eddies whose dimensions scale with distance to the wall.

The present work supports the view that the current AEM could be improved by inclusion of up-gradient transport. Eyink (2008) pointed out that the nonlinear vorticity flux obtained by matched asymptotics over the entire log layer is reproduced within the AEM as

$$\langle v\omega_z - w\omega_y \rangle \propto u_\tau^2 \left(\frac{P\delta}{y^2} - \frac{Q}{h} \right), \tag{4.1}$$

for $\delta := \nu/u_\tau \ll y \ll h$, if only one replaces the usual AEM assumption on the eddy-intensity function that $I_{xy}(y^*) \to 0$ for $y^* \gtrsim 1$ instead with $I_{xy}(y^*) \sim -P/y^*$ for $y^* \gg 1$ and P a numerical prefactor. In that case, up-gradient vorticity transport for $y < y_p := (P\delta h/Q)^{1/2}$ is correctly recovered, but the assumed decay is much slower than the rate $I_{xy}(y^*) = O(1/y^{*4})$ for $y^* \gg 1$ (see Eyink 2008 for details) obtained from the Biot–Savart formula by assuming a 'representative eddy' in the form of a hairpin line vortex (Woodcock & Marusic 2015, Appendix C). It has been an open question since Eyink (2008) what alternate vortex structure might yield such up-gradient transport. In agreement with the classic work of Kim & Moin (1986), our study suggests that the additional structures could be associated with sweeps and we identify these as 'shawl vortices'. Lighthill's hypothesis that vorticity transport toward the wall is taken over by 'smaller-scale movements' suggests another competitive direct-cascade process in which large-scale vortices are transported toward the wall, fragment into smaller structures and proliferate in number. The shawl vortices wrapped around downflows, as revealed by conditional averaging in figure 1(*b*), seem to originate above the wall but interact with it by inducing opposite-sign vorticity. These observations open up new possibilities for vortex-based structure models that may refine the AEM.

There are many possible elaborations and future directions of work. We have not fully explored the 3-D characteristics of the conditional eddies illustrated in figure 1. For example, the control-volume arguments presented in figure 5, 7 are essentially two-dimensional but the vortex lines plotted in figure 1(*a*,*b*) are streamwise inclined and

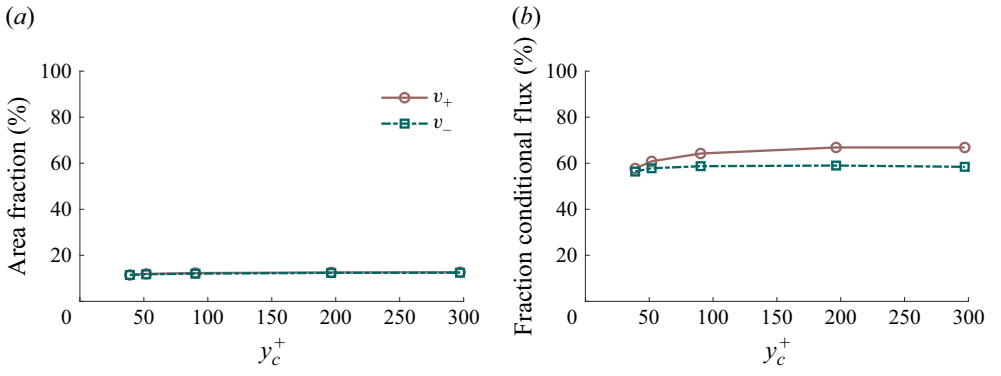

Figure 16. (*a*) Fraction of area occupied, and (*b*) contribution to conditional flux from, strong outflow events ($v > v_{rms}$) and strong inflow events ($v < v_{rms}$).

likewise the conditional flows are fully three-dimensional. Perhaps most importantly, our study supports Lighthill's suggestion of a vorticity cascade mechanism, but no strict causal connection has been established between vorticity at different scales, locations and times. A promising method to get more detailed dynamical understanding is the stochastic Lagrangian approach (Wang *et al.* 2022), especially if combined with conditional averaging. Monte Carlo evaluation of the stochastic Lagrangian trajectories is prohibitively expensive in the logarithmic layer, but a recent Eulerian adjoint vorticity algorithm (Xiang *et al.* 2025) makes this feasible. In the latter paper, Lighthill's mechanism was verified as the causal origin of strong spanwise vorticity in the viscous sublayer of turbulent channel flow. Finally, an important direction of future research is to exploit better understanding of the vorticity dynamics responsible for turbulent drag in order to develop improved drag reduction strategies (Kumar *et al.* 2025).

Supplementary material. Computational Notebook files are available as supplementary material at https://doi.org/10.1017/jfm.2025.654 and online at https://www.cambridge.org/S002211202510654X/JFM-Notebooks.

Funding. We thank the Simons Foundation for support of this work through the Targeted Grant No. MPS-663054 and Collaboration Grant No. MPS-1151713 and the National Science Foundation for funding through Grant No. CSSI-2103874.

Declaration of interests. The authors report no conflict of interest

Appendix A. Area and flux fractions of high wall-normal velocity points

The average fluxes displayed in figure 2 in the main text were conditioned simply on $v > 0$ and $v < 0$, but the definition of the conditional ensembles in § 2.2 employed a threshold magnitude of wall-normal velocity. To select an appropriate threshold, we applied conditions $v > \alpha v_{rms}$ and $v < -\alpha v_{rms}$ for various choices of the parameter α. For each choice, we calculated the fractional area occupied by points satisfying that condition in wall-parallel planes at fixed heights y_c and also the fractional contribution of those points to the mean nonlinear vorticity flux through those planes.

For the case $\alpha = 1$ shown in figure 16 we found that the points for both v_+ and v_- conditions occupy around 12 % of the area, nearly independent of y_c. On the other hand, the contribution of these points to the nonlinear vorticity flux through those planes is upward of 60 % and very slightly increasing with y_c. Thus, the flux contribution outweighs the area fraction by more than fivefold, emphasising the importance of these regions for vorticity transport. We note also that at each y_c-value there are somewhat more points

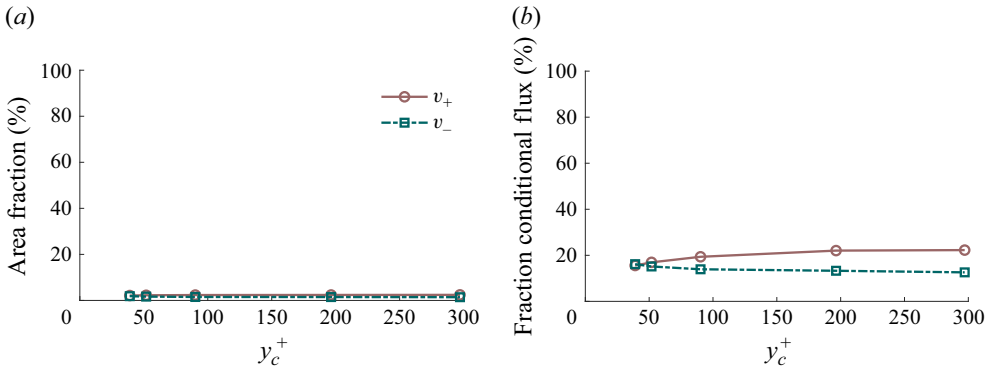

Figure 17. (*a*) Fraction of area occupied, and (*b*) contribution to conditional flux from, strong outflow events($v > 2v_{rms}$) and strong inflow events ($v < 2v_{rms}$).

satisfying the v_+ condition than the v_- condition, with the difference growing slightly as well with increase of y_c. This observation is another indication of the somewhat greater strength of outflow events than inflow events at all wall distances.

For the case $\alpha = 2$ shown in figure 17 we found that the points for both v_+ and v_- conditions occupy around 2 % of the area, again nearly independent of y_c, but the contribution to the nonlinear vorticity flux is upward of 20 % and again slightly increasing with y_c. Thus, the flux contribution outweighs the area fraction here by more than tenfold. We observe once again greater strength of outflow events than inflow events at all wall distances. Furthermore, we calculated the conditional means fields for $\alpha = 2$ analogous to those plotted in figure 4, 6, using the same methodology described in § 2.2. The results are extremely close to those presented in figure 4, 6 of the main text for $\alpha = 1$, with just somewhat greater magnitudes of all conditional mean fields.

Based on all of these observations, we decided to present in the main body of the paper results for the case $\alpha = 1$. As we have seen here, this choice of threshold was sufficiently high to obtain coherent flow structures from conditioning and, at the same time, sufficiently low to guarantee nearly complete coverage of the wall area by the sampling windows for the selected events.

Appendix B. Vortex lines in individual realisations of the conditional ensembles

At the end of § 2.2, we exhibited vortex lines for the strongest outflow (v_+) and inflow (v_-) events, as identified by our conditional sampling method in one time snapshot at $y_c^+ = 92.8$. To help give more intuition about the individual realisations of our conditional ensembles, we here plot vortex lines for additional snapshots. Furthermore, to see the variation with wall distance, we show vortex lines in figure 18 for the strongest outflow events at five wall distances distributed through the log layer in three time snapshots and in figure 19 we show vortex lines for the strongest inflow events in the same three snapshots at the same wall distances. To keep the plots simple, we show the single unique vortex line that passes through the conditioning point and projected into the yz-plane through that point.

Although vortex lines are plotted for only a few events out of the large number in the conditional ensembles (see table 1), they suggest a few general trends. First, we see that outflow events lead to hairpin-type vortices but more or less disordered by the turbulent environment and likewise the inflow events lead to inverted hairpin-type vortices. The

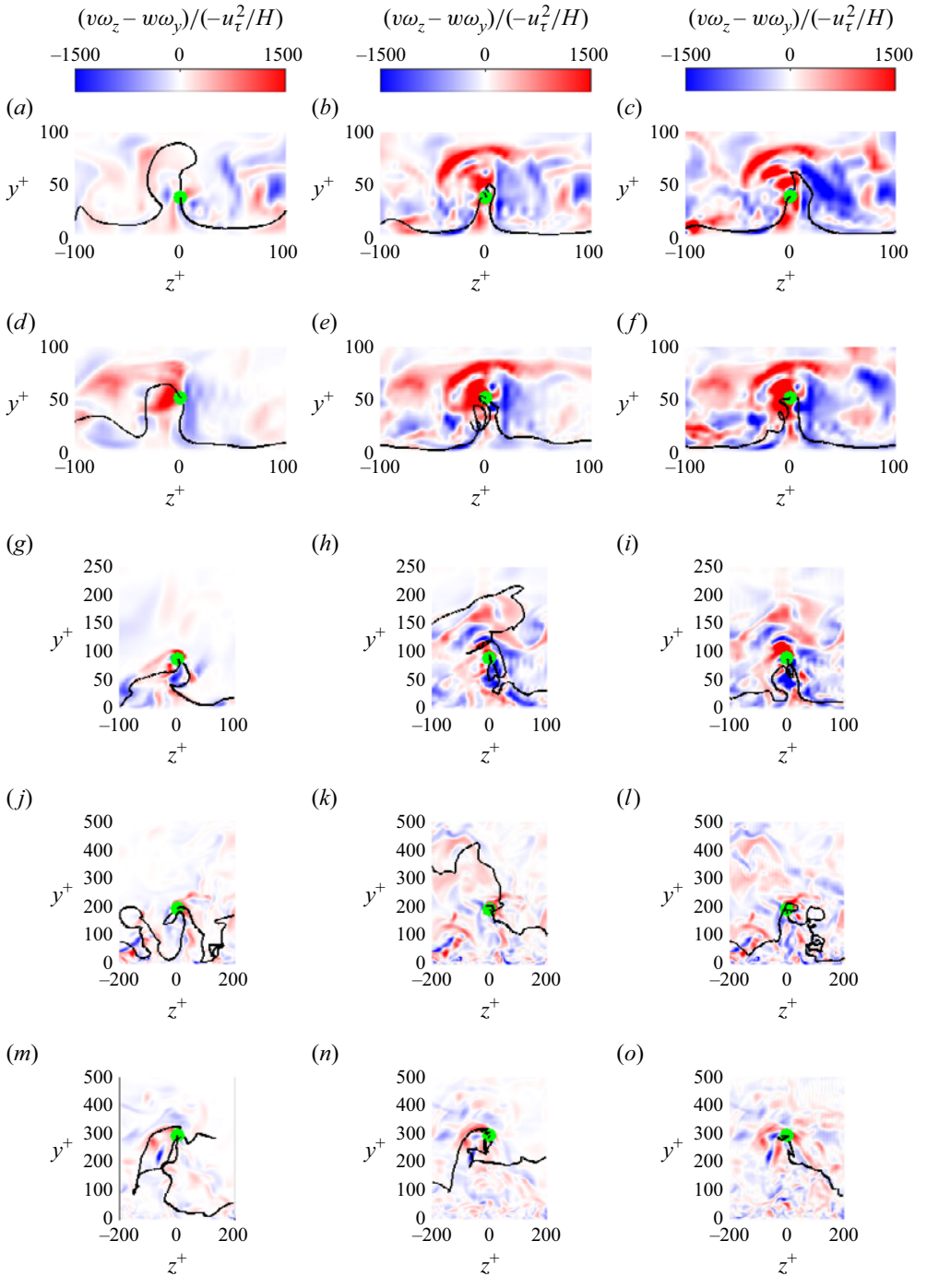

Figure 18. Vortex lines passing through the conditioning point associated with the strongest outflow events at a given wall height, at different time instants, with the background coloured by the instantaneous nonlinear flux on the spanwise–wall-normal plane passing through the conditioning point. The conditioning points are at (*a–c*)$y_c^+ = 39$, (*d–f*) $y_c^+ = 52$, (*g–i*)$y_c^+ = 92.8$, (*j–l*)$y_c^+ = 197$, (*m–o*) $y_c^+ = 298$.

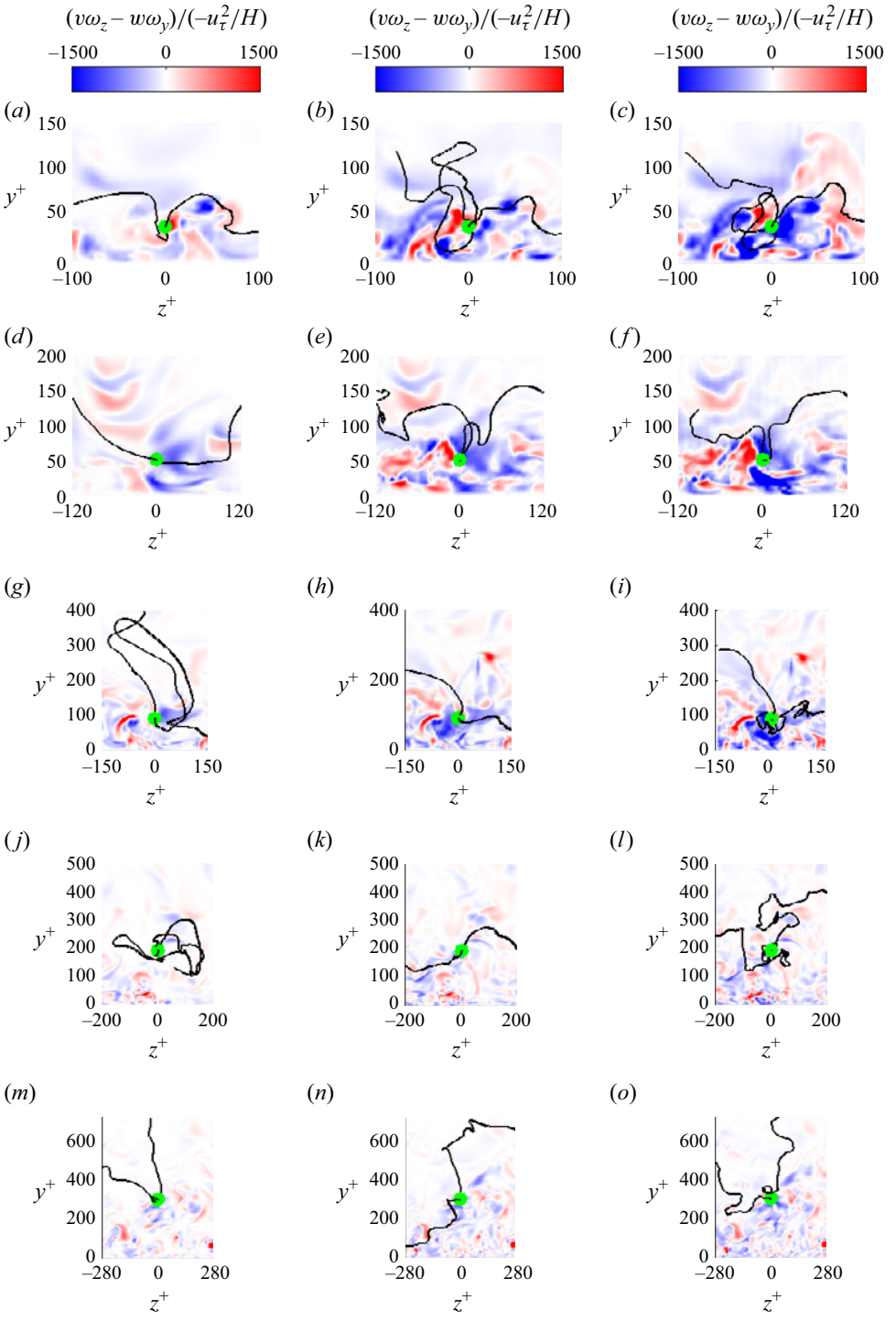

Figure 19. Vortex lines passing through the conditioning point associated with the strongest inflow events at a given wall height, at different time instants, with the background coloured by the instantaneous nonlinear flux on the spanwise–wall-normal plane passing through the conditioning point. The conditioning points are at (*a–c*)$y_c^+ = 39$, (*d–f*) $y_c^+ = 52$, (*g–i*)$y_c^+ = 92.8$, (*j–l*)$y_c^+ = 197$, (*m–o*) $y_c^+ = 298$.

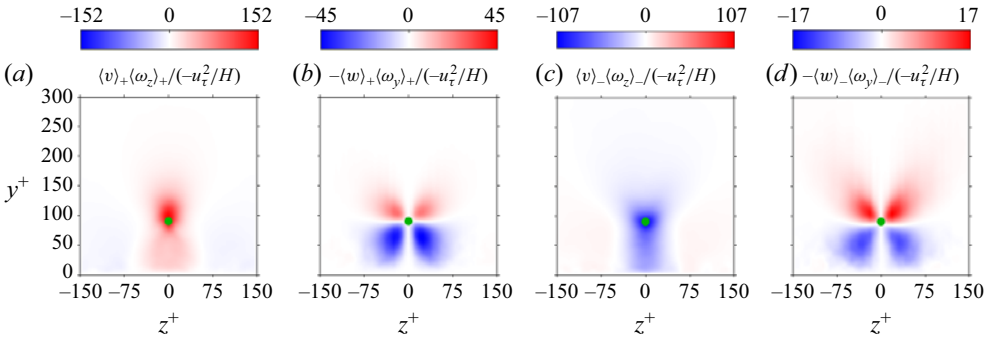

Figure 20. Vorticity-flux fields of mean eddies conditioned on the outflow/inflow events at $y_c^+ = 92.8$: the convective term for (*a*) outflow and (*c*) inflow and the stretching/tilting term for (*b*) outflow and (*d*) inflow. A green dot marks the conditioning point.

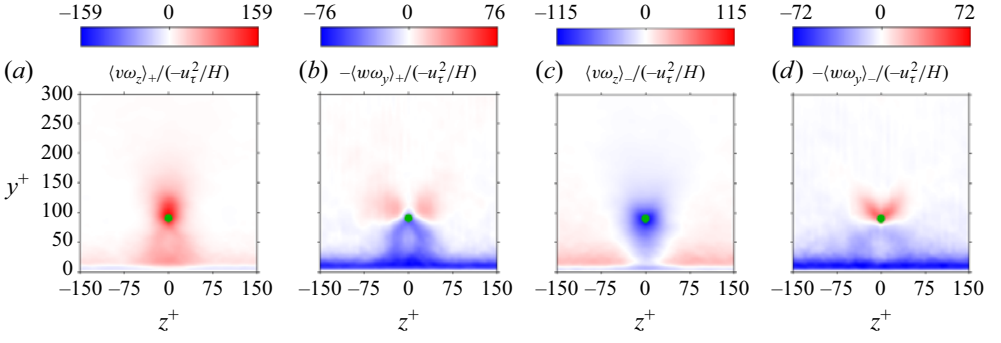

Figure 21. Mean vorticity-flux fields conditioned on the outflow/inflow events at $y_c^+ = 92.8$: the convective term for (*a*) outflow and (*c*) inflow and stretching/tilting term for (*b*) outflow and (*d*) inflow. A green dot marks the conditioning point.

vortex lines are more ordered for outflows than for inflows and also more ordered at decreasing distances from the wall.

The vortex lines through the conditioning points, as well as those at a fraction of the wall distance higher and lower, can be reconstructed from the earlier-in-time vorticity in a Lagrangian sense by the methods of Wang *et al.* (2022) and Xiang *et al.* (2025). Such reconstruction for the conditional ensembles can reveal the causal dynamics of the vorticity cascade proposed by Lighthill (1963).

Appendix C. Egligible effect of fluctuations in conditional mean fluxes

We noted in the main text at the end of § 3.2 that our successful explanation of the conditional mean vorticity flux based upon the properties of the conditional mean eddies requires that correlations of velocity and vorticity fluctuations be weak. Here, we expand on that point in some detail and we furthermore quantify the magnitude of velocity–vorticity fluctuation correlations.

In figure 20 we plot the fluxes of the conditional eddies, both convective $\langle v\rangle_\pm\langle\omega_z\rangle_\pm$ and stretching/tilting $-\langle w\rangle_\pm\langle\omega_y\rangle_\pm$, which are directly related to the conditional field lines and flows plotted in figures 4(*c*,*d*) and 6(*c*,*d*). These quantities are *a priori* distinct from the conditional mean fluxes, $\langle v\omega_z\rangle_\pm$ and $-\langle w\omega_y\rangle_\pm$, plotted in figures 4(*a*,*b*) and 6(*a*,*b*)

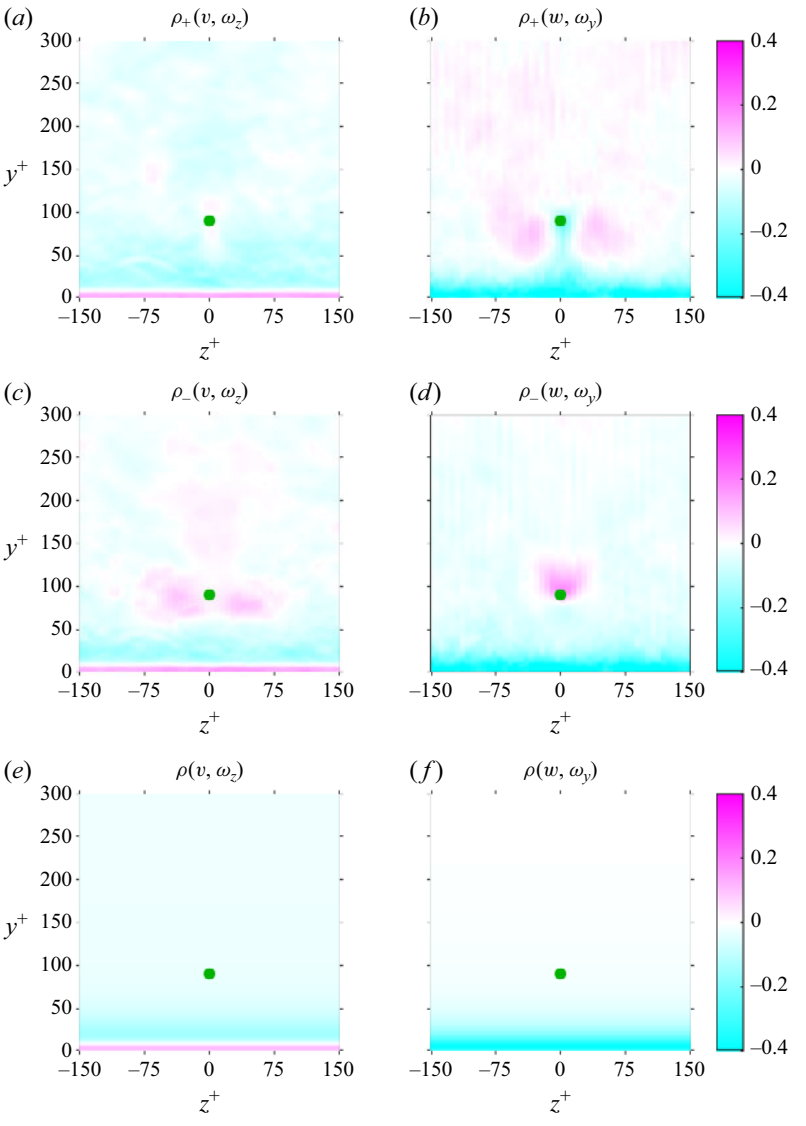

Figure 22. Correlation coefficients for the two factors in the convective term $\rho_\pm(v, \omega_z) = (\langle v\omega_z\rangle_\pm - \langle v\rangle_\pm\langle\omega_z\rangle_\pm)/v_\pm^{rms}\omega_{z\pm}^{rms}$, conditioned on (*a*) outflow and (*c*) inflow, and for the two factors in the stretching/tilting term, $\rho_\pm(w, \omega_y) = (\langle w\omega_y\rangle_\pm - \langle w\rangle_\pm\langle\omega_y\rangle_\pm)/w_\pm^{rms}\omega_{y\pm}^{rms}$, conditioned on (*b*) outflow and (*d*) inflow, at $y_c^+ = 92.8$. Also shown are the unconditioned correlation coefficients for the convective term (*e*)$\rho(v, \omega_z) = (\langle v\omega_z\rangle - \langle v\rangle\langle\omega_z\rangle)/v^{rms}\omega_z^{rms}$ and stretching/tilting term (*f*) $\rho(w, \omega_y) = (\langle w\omega_y\rangle - \langle w\rangle\langle\omega_y\rangle)/w^{rms}\omega_y^{rms}$.

in the main text and reproduced here for convenience in figure 21. Since the issues are very similar for all y_c values, we have confined the plots and discussion to the single wall-normal distance $y_c^+ = 92.8$ presented as the primary example in the main text.

Comparing the results in figures 20 and 21, we see first they are remarkably similar, except near the wall. Not only are the signs and patterns of the two sets of fluxes closely similar, but also the magnitudes are quite similar for the advective flux and differ by a factor of only 2–3 for the stretching flux. On the other hand, the conditional mean fluxes show up-gradient transport very near the wall that is missing in the flux of the conditional

eddies, especially strong for the stretching fluxes. Furthermore, this near-wall up-gradient flux is quite uniform in z and also nearly the same for outflow and inflow events. It is reasonable to expect that memory of the condition at $y_c^+ = 92.8$ fades far from the conditioning point, so that the near-wall conditional mean fluxes are presumably close to the unconditional means.

The close resemblance of the results in figures 20 and 21 requires that the fluctuation correlation coefficients of the velocity and vorticity factors in the fluxes must be small for both condition ensembles. In figure 22(*a–d*) we have plotted the Pearson correlation coefficients for both advective and stretching/titling fluxes and for both outflow/inflow. Except near the walls, the coefficients are less in magnitude than approximately 0.2, confirming the small correlations of fluctuations. The coefficients are strongest close to the wall, especially for the stretching flux where they rise to a maximum magnitude of 0.4. We have plotted also the Pearson correlation coefficients for the unconditional means in figure 22(*e*, *f*), verifying that they are nearly the same as for the analogous conditional means in figure 22(*a–d*). In the main text, we proposed that the generally weak correlations of fluctuations are due to the scale separation expected for velocity and vorticity and this explanation is consistent with the increase of correlations in the near-wall region where the separation in scales disappears.

Appendix D. Distribution of inflow and outflow events

The autocorrelation function of the normal velocity in wall-parallel planes at height y_c

$$\rho_{vv}(r_x, r_z|y_c) = \frac{\langle v(x, y_c, z, t)v(x + r_x, y_c, z + r_z, t)\rangle_{x,z,t}}{v_{rms}^2(y_c)}, \tag{D1}$$

shown in figure 23(*a*,i–v), exhibits a weak negative minimum at spanwise distance $r_z = r_m \sim 1.3y_c$ for each y_c value. This minimum implies that, on average, moving a distance $\pm r_m$ in the spanwise direction from a strong outflow (inflow) event will lead us to an inflow (outflow) event. However, the strength of the autocorrelation suggests that the inflow (outflow) event may be much weaker than the corresponding outflow (inflow) event.

On the other hand, the conditional ensembles that we have employed include only events where $|v| > v_{rms}$. A strong outflow (inflow) event included in the conditional average may or may not have an inflow (outflow) event which can be found by a spanwise shift of r_m and which is also strong enough to be included in the corresponding conditional average. In order to quantify the proportion of such reverse events which are sufficiently strong, we define the reverse event displacement vector $\boldsymbol{d}$. At a given wall-normal height y_c, for each outflow event included in the conditional average ($v(\boldsymbol{x}_p) > v_{rms}$) located at $\boldsymbol{x}_p = (x_p, y_c, z_p)$, let the nearest inflow event included in the conditional average ($v(\boldsymbol{x}_n) < -v_{rms}$)) be located at $\boldsymbol{x}_n = (x_n, y_c, z_n)$. We then define $\boldsymbol{d} := \boldsymbol{x}_n - \boldsymbol{x}_p = (x_n - x_p, 0, z_n - z_p)$, with reverse event distance $d = |\boldsymbol{d}|$ and $\theta = \arctan((z_n - z_p)/(x_n - x_p))$, the angle made by the vector $\boldsymbol{d}$ with the z axis. We posit that an inflow event can be considered a 'spanwise shift' of an outflow event if $d \leqslant r_m$ and $|\theta| \leqslant \pi/4$. The probability density function (PDF) and cumulative distribution function (CDF) of d for different y_c -values are shown in figures 23(*b*,i–v) and figures 23(*c*,i–v), with dashed pink lines marking the corresponding r_m. We see that as the wall-normal distance y_c of the conditioning point increases, the proportion of cases with $d < r_m$ also increases from 14 % for $y_c^+ = 39$ (figure 23*c*,i) to 54 % for $y_c^+ = 298$(figure 23*c*,v). Meanwhile, the PDF and CDF of θ are illustrated in figures 23(*d*,i–v) and 23(*e*,i–v) respectively, with magenta dashed curves showing the corresponding values for the cases where $d \leqslant r_m$. The plots show that overall, there is no strongly preferred direction of displacement, while the proportion of cases

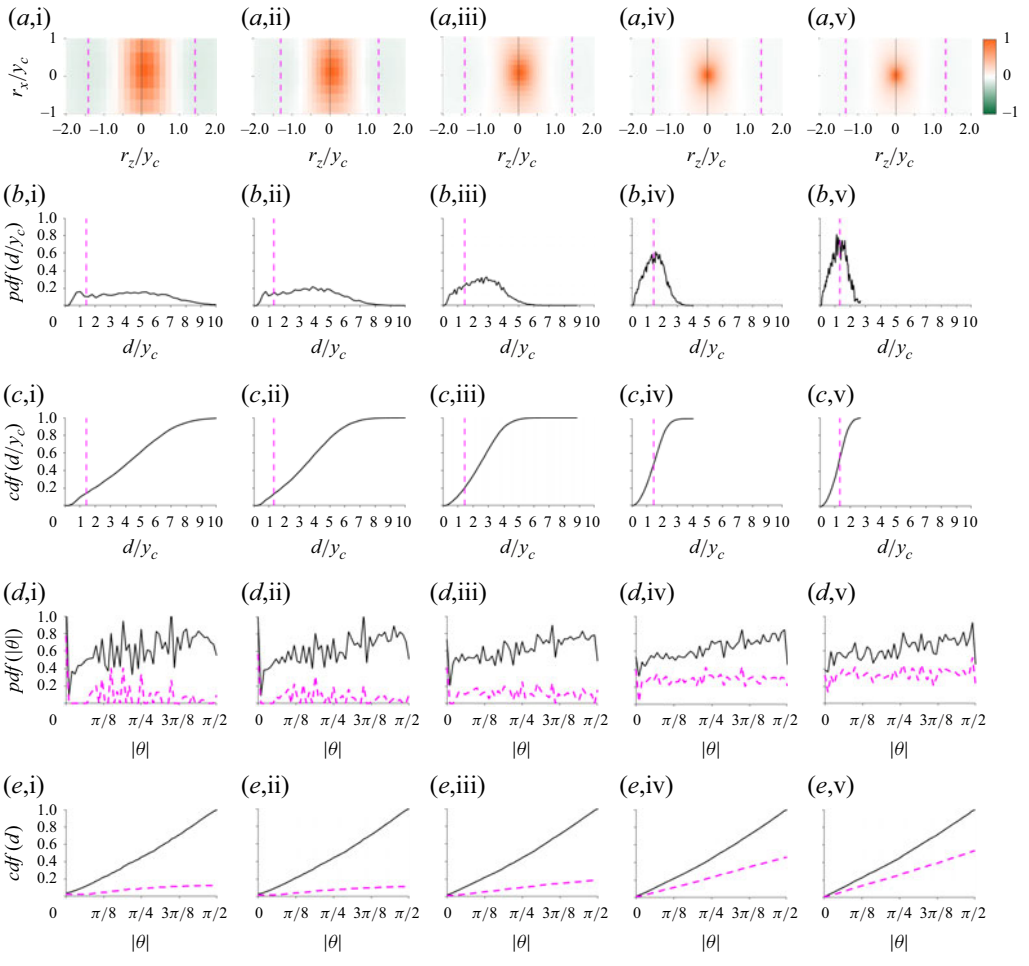

Figure 23. (*a*, i–v) Autocorrelation of wall-normal velocity $\rho_{vv}(r_x, y_c, r_z)$, magenta dashed lines mark the location of local minima, $r_z^+ = r_m^+$ and $r_z^+ = -r_m^+$. (*b*, i–v) Probability distribution function (pdf) and (*c*,i–v) cumulative distribution function of the reverse event distance $d = |\boldsymbol{d}|$, with magenta dashed lines marking respective r_m^+. (*d*,i–v) *pdf* and (*e*,i–v) *cdf* of the absolute value of the angle $|\theta|$ made by $\boldsymbol{d}$ with the z axis. Magenta dashed lines show the pdf and cdf of $|\theta|$ where $d \leqslant r_m$. The planes are at (*a–e*,i)$y_c^+ = 39$, (*a–e*,ii)$y_c^+ = 52$, (*a–e*,iii)$y_c^+ = 92.8$, (*a–e*,iv)$y_c^+ = 197$, (*a–e*,v)$y_c^+ = 298$..

which could be considered a 'spanwise shift', with $|\theta| \leqslant \pi/4$ and $d \leqslant r_m$ increases from 9 % for $y_c^+ = 39$(figure 23*e*,i) to 26 % for $y_c^+ = 298$(figure 23*e*,v).

Thus, we see that at most a quarter of the inflow events strong enough to be included in the conditional average can be considered a 'spanwise shift' of a strong outflow event. Our results show that strong outflow and strong inflow events cannot in general be identified with the adjacent reverse flows obtained from small spanwise shifts. This finding supports the idea that the ejections and sweeps identified by our criteria are not adjacent parts of the same structure, but instead different structures. It is true that small spanwise shifts from a strong outflow (inflow) event will lead to an inflow (outflow) event, but these adjacent reversed flows are generally weaker and do not satisfy the strength criterion that we impose to define our conditional ensembles.

References

Adrian, R.J., Jones, B.G., Chung, M.K., Hassan, Y., Nithianandan, C.K. & Tung, A.T.-C. 1989 Approximation of turbulent conditional averages by stochastic estimation. *Phys. Fluids A* **1** (6), 992–998.

Anderson, P.W. 1966 Considerations on the flow of superfluid helium. *Rev. Mod. Phys.* **38**, 298–310.

Brown, G.L., Lee, M. & Moser, R.D. 2015 Vorticity transport: the transfer of viscous stress to Reynolds stress in turbulent channel flow. In Ninth International Symposium on Turbulence and Shear Flow Phenomena (TSFP-9), vol. **2**. Begel House Inc.

Du, Y. & Zaki, T.A. 2025 Vorticity dynamics and drag for flows over a sphere and a prolate spheroid. *J. Fluid Mech.* **1015**, A9.

Eyink, G.L. 2008 Turbulent flow in pipes and channels as cross-stream 'inverse cascades' of vorticity. *Phys. Fluids* **20** (12), 125101.

Graham, J. *et al.* 2016 A web services accessible database of turbulent channel flow and its use for testing a new integral wall model for LES. *J. Turbul.* **17** (2), 181–215.

Gad-el Hak, M. 1990 Some unanswered questions in Fluid Mechanics. *ASME. Appl. Mech. Rev.* **43** (8), 153–170.

Huggins, E.R. 1971 Dynamical theory and probability interpretation of the vorticity field. *Phys. Rev. Lett.* **26** (21), 1291.

Huggins, E.R. 1994 Vortex currents in turbulent superfluid and classical fluid channel flow, the Magnus effect, and Goldstone boson fields. *J. Low Temp. Phys.* **96** (5), 317–346.

Hutchins, N., Monty, J.P., Ganapathisubramani, B., Ng, H.C.-H. & Marusic, I. 2011 Three-dimensional conditional structure of a high-Reynolds-number turbulent boundary layer. *J. Fluid Mech.* **673**, 255–285.

Josephson, B.D. 1965 Potential differences in the mixed state of type II superconductors. *Phys. Lett.* **16** (3), 242–243.

Kim, J. & Moin, P. 1986 The structure of the vorticity field in turbulent channel flow. Part 2. Study of ensemble-averaged fields. *J. Fluid Mech.* **162**, 339–363.

Klewicki, J.C., Fife, P., Wei, T. & McMurtry, P. 2007 A physical model of the turbulent boundary layer consonant with mean momentum balance structure. *Phil. Trans. R. Soc. Lond. A* **365** (1852), 823–840.

Kumar, S. & Eyink, G.L. 2024 A Josephson–Anderson relation for drag in classical channel flows with streamwise periodicity: effects of wall roughness. *Phys. Fluids* **36** (9), 093113.

Kumar, S., Meneveau, C. & Eyink, G.L. 2023 Vorticity cascade and turbulent drag in wall-bounded flows: plane Poiseuille flow. *J. Fluid Mech.* **974**, A27.

Kumar, S., Toedtli, S., Zaki, T.A. & Eyink, G.L. 2025 Josephson–Anderson relation as diagnostic of turbulent drag reduction by polymers. *Phys. Rev. E* **111** (1), 015105.

Li, Y., Perlman, E., Wan, M., Yang, Y., Meneveau, C., Burns, R., Chen, S., Szalay, A. & Eyink, G.L. 2008 A public turbulence database cluster and applications to study Lagrangian evolution of velocity increments in turbulence. *J. Turbul.* **9**, N31.

Lighthill, M.J. 1963 Introduction: boundary layer theory. In *Laminar Boundary Theory*, (ed. L. Rosenhead), pp. 46–113. Oxford University Press.

Lozano-Durán, A., Flores, O. & Jiménez, J. 2012 The three-dimensional structure of momentum transfer in turbulent channels. *J. Fluid Mech.* **694**, 100–130.

Marusic, I. & Monty, J.P. 2019 Attached eddy model of wall turbulence. *Annu. Rev. Fluid Mech.* **51**, 49–74.

Taylor, G.I. 1932 The transport of vorticity and heat through fluids in turbulent motion. *Proc. R. Soc. Lond. A* **135** (828), 685–702.

Tennekes, H. & Lumley, J.L. 1972 *A First Course in Turbulence*. MIT Press.

Terrington, S.J., Hourigan, K. & Thompson, M.C. 2021 The generation and diffusion of vorticity in three-dimensional flows: Lyman's flux. *J. Fluid Mech.* **915**, A106.

Townsend, A.A. 1976 *The Structure of Turbulent Shear Flow*, 2nd edn. Cambridge University Press.

Wang, M., Eyink, G.L. & Zaki, T.A. 2022 Origin of enhanced skin friction at the onset of boundary-layer transition. *J. Fluid Mech.* **941**, A32.

Willmarth, W.W. & Lu, S.S. 1972 Structure of the Reynolds stress near the wall. *J. Fluid Mech.* **55** (1), 65–92.

Woodcock, J.D. & Marusic, I. 2015 The statistical behaviour of attached eddies. *Phys. Fluids* **27** (1), 015104.

Xiang, T., Eyink, G.L. & Zaki, T.A. 2025 The origin of vorticity in viscous incompressible flows. *J. Fluid Mech.* **1011**, A33.